Seasonal Temperature Variability in the Upper Southwest Pacific Ocean

NEIL J. HOLBROOK

School of Earth Sciences, Macquarie University, North Ryde, New South Wales, Australia

NATHANIEL L. BINDOFF

Antarctic CRC, University of Tasmania, Hobart, Tasmania, Australia

(Manuscript received 3 February 1997, in final form 12 March 1998)

ABSTRACT

Climatological monthly upper-ocean temperature anomalies from the annual mean in the subtropical southwest Pacific Ocean show a characteristic out-of-phase relationship between the mixed layer and the underlying water. The mixed layer temperature anomalies in the subtropical gyre and midlatitudes are consistent in the spatial distribution and phase expected from solar radiation. However, below the mixed layer, the temperature anomalies between 10°S and 30°S are coherent throughout the water column to 450-m depth and are almost 180° out of phase with the mixed layer temperatures. This pattern of temperature anomalies describes vertical movements of the thermocline more closely linked to the seasonal variations in the wind stress curl.

To test this hypothesis, a one-dimensional linear vorticity model was forced using the Hellerman and Rosenstein monthly wind stresses across the entire width of the South Pacific Ocean. This simple wind-driven model has considerable skill in predicting the gyre-scale pattern of change in the phase and amplitude associated with thermocline variations in the subtropical gyre. Experiments, varying the Rossby wave speed, showed that a better representation is achieved with speeds of 2 to 2.5 times that observed from altimeter observations. Overall, the inclusion of long Rossby waves appears to be a very important contribution to the amplitude of the thermocline depth variations in the southwest Pacific. Furthermore, this important Rossby wave contribution is supported by the large-scale anomaly patterns obtained from more sophisticated three-dimensional dynamical ocean models.

1. Introduction

Most oceanographic work in the southwest Pacific has focused on either the East Australian Current (EAC) (Hamon 1965; Godfrey et al. 1980; Boland and Church 1981; Church and Boland 1983; Church 1987), the Tasman Front (Andrews et al. 1980; Mulhearn 1987), mesoscale eddies shed by the EAC (Mulhearn et al. 1986; Lilley et al. 1986; Mulhearn et al. 1988), or on the large-scale *steady* circulation within the region (Wyrtki 1962; Ridgway and Godfrey 1994). These studies have shown that the EAC and the Tasman Front are constantly meandering and shed discrete eddies. The frequency of discrete eddy formation from the EAC is about two per year and appears to be related to the seasonal cycle (Godfrey et al. 1980). Calculations of the strength of the EAC from wind stress data using the Sverdrup balance indicates that the EAC has a net transport of about 25 Sv (Godfrey 1989). However, this transport is weak when compared with the transport of the other western boundary currents such as the Gulf Stream, the Kuroshio, and the Agulhas.

The apparent seasonality in the strength of the EAC and the generation of mesoscale eddies has implications for the large-scale structure of the subtropical gyre (15°–40°S) and for the circulation in the equatorial region and Coral Sea. Seasonal changes in the transport of the EAC implies that there has been an adjustment of the subtropical gyre and that this adjustment must be reflected in temperature anomalies within the water column.

In this paper, we focus on the seasonal cycle of the depth variations of the thermocline across the southwest Pacific derived from existing bathythermograph data for the period 1955 to 1988. This emphasis on the gyre-scale seasonal cycle has several distinct advantages. First, the distribution of the historical data favors the examination of large-scale variations rather than the shorter scales in time and space that are required to study the EAC directly.

Second, large-scale seasonal variations in sea surface heights can now be sampled globally by satellite altimeters such as the TOPEX/Poseidon satellite (Stammer and Wunsch 1994; Minster et al. 1995). It is of interest, therefore, to understand and evaluate the vertical chang-

Corresponding author address: Dr. Neil Holbrook, School of Earth Sciences, Macquarie University, North Ryde, NSW 2109, Australia. E-mail: Neil.Holbrook@mq.edu.au

es in temperature (and salinity) implied by the sea surface height measurements from this satellite. Such internal changes in the temperature field describe the baroclinic component of the altimeter height variations and is important for assimilation techniques that depend on vertical extension schemes that propagate information from the sea surface to the bottom of the ocean (De Mey and Robinson 1987; Haines 1991).

Third, due to the large spatial scales, it is possible to examine the dynamical processes that drive the thermocline variations using a simple wind-driven model. For the subtropical gyre, where this model is found to be appropriate, we are able to explore the role of local forcing, through Ekman pumping, and the role of Rossby waves on the seasonal cycle of the thermocline.

The structure of this paper is as follows. Section 2 describes the data analysis, section 3 presents the results of the data analysis, section 4 the comparison of the observed thermocline variations with a simple wind-forced model, and section 5 is the final discussion.

2. Data and analysis

The ocean temperature data used in this study are from the archives of the National Oceanographic Data Center (National Oceanographic Data Center 1991) and represent the most comprehensive compilation of oceanographic measurements available for this region. A total of almost 40 000 mechanical and expendable bathythermograph (MBT and XBT) casts are included in this analysis of the temperature data for the southwest Pacific region between 0° and 50°S, 140°E and 180° during the period from 1955 to 1988. The distribution of these data, after quality control, is shown in Figs. 1 and 2. Given the large number of observations and the limitations of computer resources, the data handling was made much more convenient by subdividing the original dataset. Based on the general circulation pattern in the region and the amount of data reduction required, four subregions were selected with reference to the local dynamics. Further, since the focus of this paper is on the large-scale seasonal variations across the region, and since the data near the East Australian coast are strongly affected by mesoscale eddies, which are noise in the analysis, the observations between 30° and 37°S and eastward from the East Australian coast to 154°E, were not included in the study. Since a major aim of this study was also to produce regularly gridded maps of the temperature distribution over the data domain, these subregions were chosen to contain a 2° overlap at each of the north–south and east–west boundaries that would ensure continuity of the mapped isotherms across the boundaries. A complete description of the data, quality checks, and data preparation are provided in Holbrook (1994).

The upper-ocean temperature measurements are four-dimensional, but are irregularly distributed in space and time. First, the bathythermograph profiles were linearly

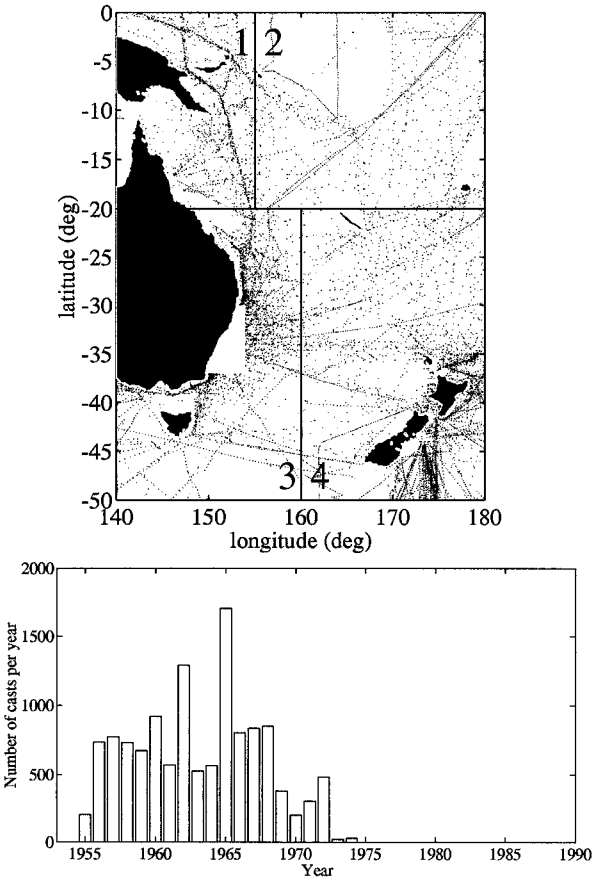

FIG. 1. Spatial positions and frequency histogram of all MBT casts retained after quality control of the data. Individual subregions are numbered accordingly while their boundaries are defined to overlap one degree beyond their respective marked bounding lines.

interpolated at 5-m depth intervals. Second, in order to homogenize these unevenly distributed ocean temperature data, they were optimally interpolated onto a regular grid in space and time. The spatial grid is the same as that for the Comprehensive Ocean–Atmosphere Data Set (Woodruff et al. 1987), that is, $2° \times 2°$, while the temporal grid points were centered on each month. The mapping of the ocean temperature data in time and space was performed using a combination of empirical orthogonal functions (EOFs) and objective mapping. This approach follows the methods used by Fukumori and Wunsch (1991) and Bindoff and Wunsch (1992) in their analysis of hydrographic data.

The procedure for interpolating the data and producing the monthly gridded climatology involves the following steps. First, the temperature profiles were organized into 12 individual monthly groups identified by each ''365.25/12 day'' month. Essentially, all January data were organized into one group, all February data into another group, and so on. Second, the EOFs of the vertical structure of the temperature data were determined and only the significant modes retained. Third,

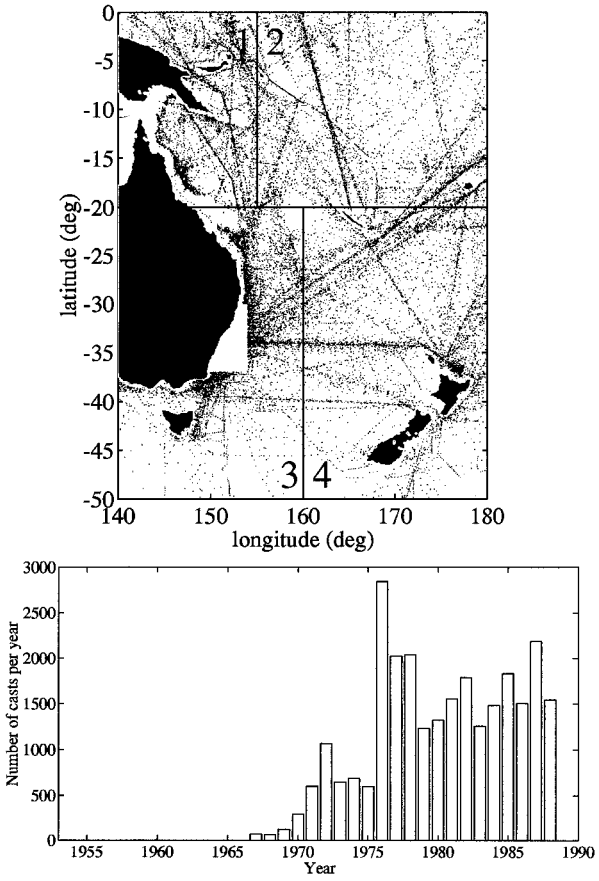

FIG. 2. Spatial positions and frequency histogram of all XBT casts retained after quality control of the data. Individual subregions are numbered accordingly and their boundaries are defined to overlap one degree beyond their respective marked bounding lines.

the corresponding spatial–temporal modes, associated with the position in time and space of each MBT/XBT profile, were objectively mapped onto both their data positions (for statistical reliability checks) and onto the regular grid. It was found here that only a small number of significant EOFs needed to be mapped. Finally, the gridded temperature field was reconstructed at each grid point (with errors) by expanding the mapped EOFs by their coefficients.

The data matrix used in the EOF procedure consisted of normalized differences between the temperature data and the a priori mean (see appendix). Here, the a priori mean field was modeled as a second-order polynomial in latitude and depth and an annual and semiannual harmonic fit in time. The normalization factor used in the EOF procedure was the estimate of the a priori noise (see appendix). The a priori noise represents the noise associated with the unresolved physical processes such as internal waves and mesoscale eddies and other sources of noise that occur with instrument type and reporting technique.

The objective mapping of the data used a zonal scale of 4°, a meridional scale of 2°, and a timescale of 90 days. The longer zonal length scale was used because the ocean temperature field is quasi zonal in this region. This choice of scales is consistent with the data distribution in time and space over the observation period. The objective mapping procedure also gives an objective estimate of the random error at each grid point. This error estimate takes into account variations in data density caused by, for example, changes in ship routing. The final gridded temperature field is a monthly climatology determined from all of the available data, in 5-m depth intervals, to 450-m depth.

Statistical checks of the objective mapping were performed to ensure that the residuals were unbiased and consistent with the a priori noise (Holbrook 1994). It was found that the vertical structure of the temperature data could be described to within the noise using only five EOFs, which explained more than 90% of the total variance in the data for each subregion. This small number of required modes shows that the vertical temperature profiles contain strong vertical correlations. Consequently, computing time was reduced by a factor of 36, resulting from the objective mapping of only five modes instead of the original 91 vertical levels, that is, a reduction of 18 times each for mapping onto the original data positions and the model grid. After objectively mapping the temperature data in the four subregions, the subregions were blended to produce the full southwest Pacific region dataset by averaging the data across the 2° overlapping boundaries. For a more detailed description of the various components of the analysis procedure see the appendix.

In summary, the EOF analysis not only reduced the data to only five modes explaining most of the overall variance, but it was also successful in identifying the relevant physical scales of both shallow and deeper depths. It should be noted that a form of EOF analysis (rotated principal components analysis) has also been applied to the uniformly gridded temperature *time series,* that is, the time history of temperature changes over the entire 1955–88 period in the southwest Pacific region. That particular study provided information about the important spatial and temporal patterns of interannual variability in the region derived from the same set of temperature observations (Holbrook and Bindoff 1997).

3. Observed seasonal variability

a. Wind stress curl

The monthly mean vertical wind-stress curl fields were calculated by taking finite differences of the monthly mean wind stresses from Hellerman and Rosenstein (1983). Figure 3 shows the wind-stress curl anomalies across the *entire* South Pacific Ocean for the months of February and June when the local wind stress curl anomalies are at their peak amplitudes in the gyre

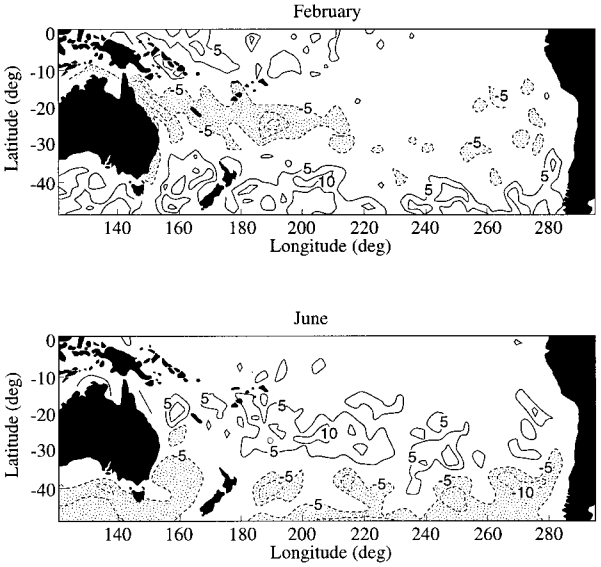

FIG. 3. Monthly mean wind-stress curl anomalies from the annual mean across the South Pacific Ocean for the months of February and June. Wind stress curl anomalies are in units of 10^{-8} N m^{-3}.

region of the southwest Pacific. During both of these months, it is clear that the large band of anomalies extends in a west-northwest to east-southeast orientation across the subtropics and into the central eastern Pacific. The positive wind stress curl observed over the subtropics of the southwest Pacific Ocean is continually

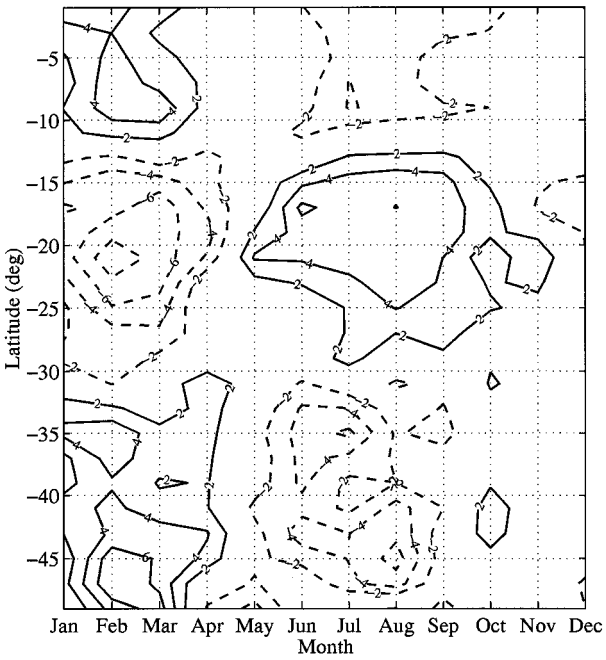

FIG. 4. Hovmöller plot of zonally averaged anomalies of the monthly mean wind stress curl from the annual mean over the southwest Pacific Ocean for each month of the seasonal cycle. Wind stress curl anomalies are in units of 10^{-8} N m^{-3}.

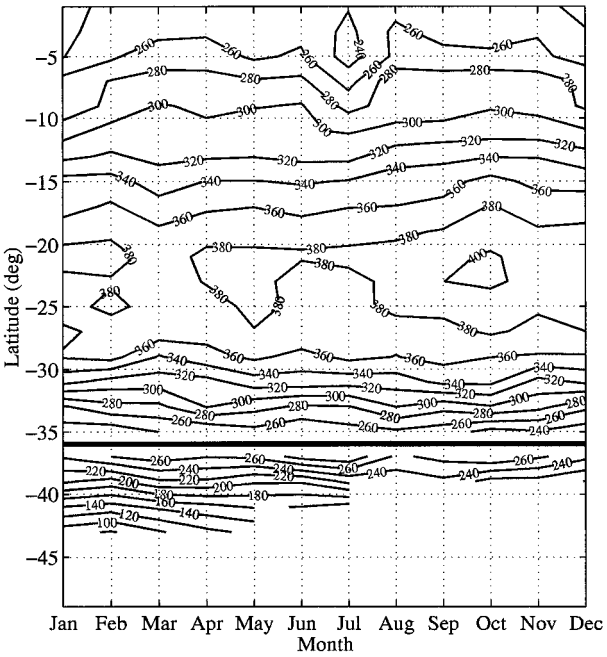

FIG. 5. Hovmöller plot of monthly and zonally averaged depths of the 14°C isotherm (equatorward of 36°S) and 13°C isotherm (poleward of 36°S) in the southwest Pacific Ocean. Depths are in meters.

forcing downwelling in the center of the gyre. Between 10° and 30°S, the wind stress curl changes sign during the seasonal cycle. These sign reversals are associated with the north–south excursions of the southeast trade wind maximum during the year.

Figure 4 shows a Hovmöller plot of the climatological monthly wind stress curl anomalies from the annual mean, zonally averaged across the southwest Pacific Ocean region. These zonal averages of the data are across ocean points only: that is, from either the eastern coastlines or western boundary of the southwest Pacific Ocean region (141°E), across the southwest Pacific basin (as defined by the boundaries shown in Figs. 1 and 2). In the subtropics (15°–30°S), the maximum negative wind stress curl anomalies occur during February while the maximum positive wind stress curl anomalies occur from June to August. South of 30°S there is almost a 180° change of phase in the wind stress curl anomalies.

b. Subsurface thermal variability

The observed seasonal variability of the depth of the thermocline in the southwest Pacific, as calculated from the monthly climatological temperature atlas, is presented. These variations are examined primarily through variations in the depth of the 14°C (D14°C) isotherm. This isotherm is used as a proxy for the depth of the pycnocline and is a reasonable choice of isotherm for the Tropics and subtropics (e.g., Meyers 1979). However, near 35°S, the 14°C isotherm rapidly approaches the surface (Fig. 5). Thus, for latitudes poleward of

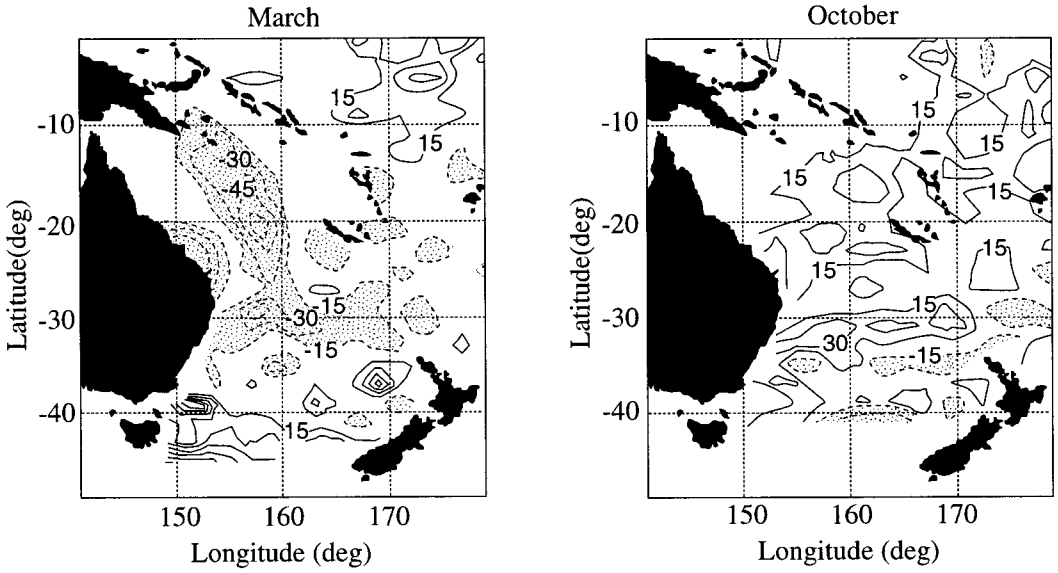

FIG. 6. Climatological Mar and Oct anomalies, from the annual mean, of the depths of the 14°C isotherm (equatorward of 36°S) and 13°C isotherm (poleward of 36°S) in the southwest Pacific Ocean. Depth anomalies are in meters and positive anomalies indicate that the isotherms are deeper.

35°S, this choice of isotherm is unsuitable. From close examination of the temperature data, it was found that the 13°C isotherm was the most suitable isotherm for representing the thermocline at these latitudes. Although we have used two specific isotherms here to represent thermocline motions, the seasonal atlas shows that below the mixed layer the temperature changes are vertically coherent over the entire depth range of the XBT data.

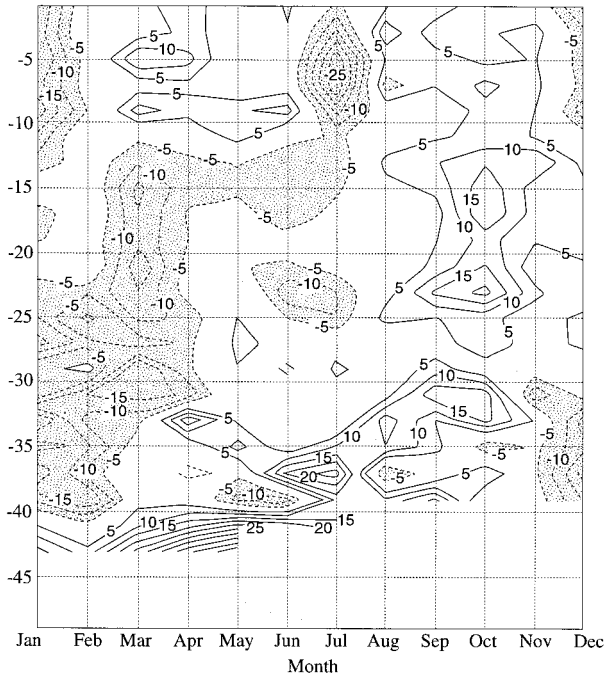

FIG. 7. Hovmöller plot of monthly and zonally averaged anomalies, from the annual mean, of the depths of the 14°C isotherm (equatorward of 36°S) and 13°C isotherm (poleward of 36°S) in the southwest Pacific Ocean. Depth anomalies are in meters and positive anomalies indicate that the isotherms are deeper.

The variability in the depth of the thermocline (i.e., D14°C/D13°C anomalies) in the southwest Pacific Ocean region has large spatial scales (Fig. 6). These scales are larger than the scales used in the objective mapping. For the subtropics, a very coherent pattern between 10° and 30°S of negative D14°C anomalies during March indicates that the thermocline is raised in late summer to early autumn; that is, the subsurface temperatures are *cooler* than the annual average during this time. Conversely, in October, the D14°C anomalies in this region indicate that the thermocline is depressed in mid spring; that is, the subsurface temperatures are *warmer* than the annual average during this time.

The most coherent changes in the depth of the D14°C isotherm occurs over the main part of the subtropical gyre in this region (cf. Fig. 5). Furthermore, the sign of the depth changes for the peak months of March and October (Fig. 6) remains the same across the entire gyre region for which data are available, whereas the longitudinal shape of the anomalies suggests that the zonal scales are at least the 30° of longitude encompassing the southwest Pacific basin (with the main peak structure extending over about 15° of longitude). Because of these long zonal scales, the seasonal pattern is presented as a simple Hovmöller plot (Fig. 7) of zonally averaged depth anomalies. The maximum amplitudes in the depth of the thermocline for the subtropics (15°–25°S) are observed during March (−15 m) and October (+15 m)

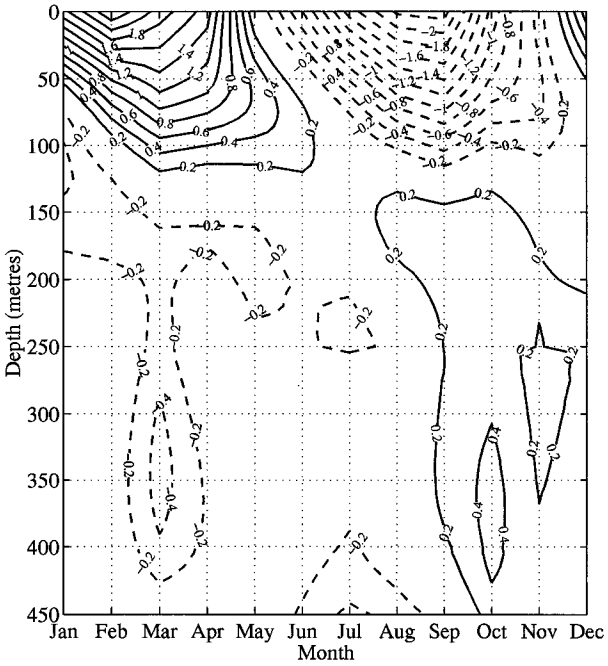

FIG. 8. The vertical structure of zonally averaged monthly mean temperature anomalies, to 450-m depth, along 19°S in the western Pacific Ocean. Temperature anomalies are in degrees Celcius.

with a smooth transition between these two periods. The pattern is represented by a single seasonal harmonic with only the slight suggestion of a semiannual period. South of 30°S, the maximum amplitudes in the depth of the thermocline tend to occur earlier in the year than at lower latitudes, with the thermocline shallowest in January/February and deepest in July/August. North of 10°S, the seasonal cycle is dominated by a semiannual period.

The difference between the mixed-layer seasonal cycle and the seasonal cycle of the depth of the thermocline is best shown in a Hovmöller plot of the vertical temperature structure near the middle of the subtropical gyre (Fig. 8). Here, the zonally averaged monthly mean temperature anomalies to 450-m depth along 19°S in the southwest Pacific indicate that warm mixed layer anomalies occur during the austral summer and autumn (December to May) extending to the base of the mixed layer (to about 100-m depth). The temperature changes observed in the surface mixed layer during the year are in phase with, and are dominated by, the seasonal cycle of solar insolation for the Southern Hemisphere. However, below the mixed layer, the zonally averaged temperatures are observed to be as much as 0.4°C less than the annual mean during March (early autumn) at depth 300–400 m. The mixed layer is cooled during the winter months (June–August) with the upper 100 m being cooler than the annual mean through to October–November (late spring). Despite the upper-ocean cool anomalies extending to about 100-m depth during this time as a result of winter convection, warm anomalies of from 0.2°–0.4°C are observed between 100-m and 450-m depth, with maximum values during October at depth 300–400 m. Since air temperatures are at a maximum in mid–late summer (January–February) and are at a minimum in mid–late winter (July–August), these subsurface temperature changes over the main part of the subtropical gyre are almost 180° out of phase with the annual insolation cycle for the Southern Hemisphere. Furthermore, the vertical extent of the temperature changes along 19°S are coherent to 450-m depth, and probably extend to deeper depths. Thus, these thermocline variations are likely to be associated with the gravest baroclinic modes.

Comparison of the D14°C anomalies with the local surface wind stress curl anomalies in the center of the subtropical gyre (10°–30°S) indicates that there is approximately a three-month lag of the vertical excursions of the thermocline from the corresponding changes in the wind stress curl. The phase of the depth variations of the thermocline in this region is consistent with the pumping of the thermocline by the surface winds. In contrast, south of 30°S, the thermocline depth (and subsurface temperature) anomalies are about 180° out of phase with the local wind stress curl. Equatorward of 10°S, there appears to be a semiannual cycle of the thermocline fluctuations and an annual cycle of the local winds.

In summary, the most likely candidate for causing the thermocline fluctuations within the subtropical gyre appears to be wind forcing over the central part of the gyre. However, the lack of correlation of the local winds with the thermocline displacements poleward of 30°S and equatorward of 10°S suggests that the dynamics involved in these regions is not simply Ekman pumping.

c. Dynamic height and sea level changes

Monthly dynamic height changes referenced to 450-m depth were also made using a uniform salinity of 35 psu. These calculations do not take account of the positive correlation between temperature and salinity in this depth range and, since the salinity–temperature correlation is positive in the Tasman Sea (Boland 1971; Pearce 1981; Reid 1986), it is likely that these dynamic heights are overestimated by a factor between 1 and 2.

As expected, the monthly and zonally averaged surface dynamic-height anomalies (not shown) with respect to 450-m depth change *in phase* with the heat content of the mixed layer, which is 90° phase lagged with seasonal solar heating over most of the southwest Pacific region, but has an increasing lag toward the higher latitudes. These surface dynamic height variations are locally consistent with monthly averaged tide gauge records from the Permanent Service for Mean Sea Level (PSMSL) (Woodworth 1991) for various sites across the southwest Pacific including Honiara (Solomon Islands) and Noumea (New Caledonia) where sea level similarly varies in phase with solar heating.

Although sea-level (and surface dynamic height) variations have been reported to be a useful measure of thermocline depth fluctuations in the tropical Pacific to 15°S (Rebert et al. 1985), for the subtropical latitudes and midlatitudes of the Coral and Tasman Seas, monthly anomalies of surface dynamic height are a poor diagnostic of the large-scale dynamic response of the thermocline to changes in the wind stress curl. The dynamic height variations for deeper depths below the mixed layer (not shown), in particular the dynamic height changes just below the base of the mixed layer (100 m) relative to 450-m depth (±4 cm over the seasonal cycle), are very similar to the pattern of D14°C/D13°C fluctuations (Fig. 7) for the region. This suggests that in order to properly understand variations in the upper-ocean thermal structure for the subtropical–middle latitudes of the southwest Pacific, in particular the dynamic variability of the thermocline, it is necessary to examine the dynamic height variations *below* the mixed layer, rather than the variations at the surface. Consequently, most of the thermal contribution to the surface dynamic height field relative to 450-m depth is through seasonal solar radiation warming of the surface mixed layer and, hence, the dynamic contribution of the winds to the temperatures below the mixed layer and to steric sea level is masked.

4. Dynamical model representations

a. Linear vorticity model simulations

Based on the analysis of the observations presented in the previous section, it is apparent that the thermocline depth variability on seasonal timescales in the southwest Pacific is unrelated to the exchange of heat into the mixed layer and is probably a dynamical response to the large-scale wind field. In order to understand the observed seasonal variability of the depth of the thermocline in this region, in terms of the relative contributions from both the *local* and *remote* wind forcing, a simple one-dimensional linear vorticity model has been used. This model is an appropriate choice for the Tropics and subtropics where the vertical density (here, the temperature) structure is approximated as an active upper layer, separated by an interface (pycnocline) from the deep motionless ocean.

From linear theory, Philander (1979) and previous investigators have shown that for wind forcing with periods of less than 1 yr, the steady-state Sverdrup balance cannot be achieved in the Pacific Ocean. On these timescales, a slightly more sophisticated model of the ocean circulation is required. Here, this model is based on the linear vorticity equation

$$\left(\nabla^2 - \frac{f^2}{c^2}\right)\frac{\partial \psi}{\partial t} + \beta\frac{\partial \psi}{\partial x} = (\nabla \times \tau)_z, \qquad (1)$$

where ψ is the mass (or volume) transport streamfunction measured in Sverdrups (1 Sv $\approx 10^9$ kg s^{-1}), $c = \sqrt{gh_{eq}}$ is the reduced-gravity wave speed, h_{eq} is the equivalent depth of the ocean layer, f is the Coriolis parameter, $\beta = \partial f/\partial y$ is the gradient of the Coriolis parameter with latitude, $(\nabla \times \tau)_z$ is the vertical component of the curl of the wind stress (τ) and x and t denote longitude and time, respectively. The long Rossby wave speed is given by $C_R = \beta c^2/f^2$ (Meyers 1979; Kessler 1990). For this model of the ocean, the equivalent depth is given by $h_{eq} = (\Delta\rho/\rho_0)h_1$, where $\Delta\rho$ is the density difference between the upper and lower layers and h_1 is the mean depth of the upper layer.

The monthly mass transport streamfunction anomalies from the model can be used to predict the expected excursions of the internal surface (thermocline). These model predictions can then be used for direct comparison with the observations. The change in height (when z is positive upward) of the internal and free surfaces are easily found using the relationships

$$\Delta\eta_{\text{internal}} = -\frac{f}{\rho c^2}\Delta\psi \qquad (2)$$

$$\Delta\eta_{\text{surface}} = -\frac{c^2}{gh_1}\Delta\eta_{\text{internal}}. \qquad (3)$$

The above equations are only valid for a motionless lower layer, whereas the mean depth of the active upper layer in the calculation is here taken to be the typical value of 300 m (Tomczak and Godfrey 1994, p. 37).

As shown in the previous section, the seasonal thermocline variability has large zonal and meridonal scales greater than 10° lat. Using simple scaling arguments, it can be shown that the dispersion term [i.e., the Laplacian term in Eq. (1)] can be neglected. For zonal length scales of $\Delta x \approx 10^6$ m (i.e., one-third of the width of the study region) and meridional length scales of $\Delta y \approx 10^6$ m (i.e., about 10° lat), the Laplacian term is two orders of magnitude smaller than the stretching term, f^2/c^2. Thus, the dispersion of the Rossby waves can be neglected and the essential physics for the time and space scales of interest to the observations is represented by the nondispersive long-wave approximation of Eq. (1) given below

$$-\frac{f^2}{c^2}\frac{\partial \psi}{\partial t} + \beta\frac{\partial \psi}{\partial x} = (\nabla \times \tau)_z. \qquad (4)$$

For this model of the ocean, a single boundary condition is imposed on the streamfunction such that there is no flow through the eastern boundary. The numerical solution to this simplified form of the vorticity equation [Eq. (4)], in one spatial dimension (longitude) and time, is solved in this study using a two-step Lax–Wendroff scheme, which is accurate to second order.

Equation (4) has two important features. It retains the effect of long Rossby waves forced by the winds outside and inside the study region and also includes the effect of the Ekman velocity (i.e., local wind forcing) on the thermocline. In the case where β is zero, Rossby waves are not supported, and this equation reduces precisely

to the Ekman velocity of the pycnocline. Thus, where β is small this equation only represents the effect of the local winds.

The model involves a number of unknown parameters all of which are linked. They are the upper-layer depth h_1, the density difference between the layers $\Delta\rho$, the first baroclinic mode gravity wave speed c_1, and the long Rossby wave speed C_R. Because of the relationship between these variables there is only one truly free parameter, and in this paper we have used the first-mode baroclinic gravity wave speed, c_1.

Based on recent global studies of theoretical and observed long oceanic Rossby waves, the zonally averaged values of C_R used in the vorticity model have been approximated from satellite altimeter observations (Chelton and Schlax 1996; Chelton et al. 1998). Since the vorticity model depends on the first-baroclinic-mode gravity wave speed, $c_1(\varphi)$, we define a set of *effective* gravity wave speeds, as a function of latitude determined directly from the observed long Rossby wave speeds [Fig. 5b of Chelton and Schlax (1996)].

Figure 9 shows the representation of both the zonally averaged theoretical and observed long Rossby wave speeds (cf. Chelton and Schlax 1996) and theoretical (cf. Chelton et al. 1998) and *effective* gravity wave speeds. The gravity wave speeds have a maximum in the middle of the subtropical gyres where they exceed 4 m s^{-1}. For Rossby waves forced with a period of 1 yr, the wavelength of these waves is a very significant proportion of the study region. For example, using the *observed* Rossby wave speeds, C_R, determined from the TOPEX/Poseidon satellite altimeter (Chelton and Schlax 1996), the wavelength is 1615 km at 35°S and 6550 km at 11°S. This compares with the width of the study region of approximately 3000 km.

Numerical experiments with the model using the observed altimeter-derived phase speeds provide fair agreement with the phase and amplitude of the temperature observations presented earlier. The inclusion of long Rossby waves (at the observed Rossby wave speeds) in the model solution for the gyre region, produces a slight increase (e.g., ±2 m along 19°S) in the seasonal range of the internal surface depth variations for the southwest Pacific that more closely represents the observed D14°C variations in this region. However, the improvements caused by including Rossby waves is still insufficient to explain the larger magnitude of the observed anomalies in this region. Although the wavelength of these baroclinic Rossby waves is a significant fraction of the region, the wavelength of these observed Rossby waves is too short, particularly at the higher latitudes, to reproduce the large zonal changes in the depth of the thermocline seen in the observed monthly temperature climatology.

We interpret this mismatch between the vorticity model simulations, using the altimeter-derived phase speeds, and the observed changes in the thermocline depths as requiring an increase in the apparent Rossby

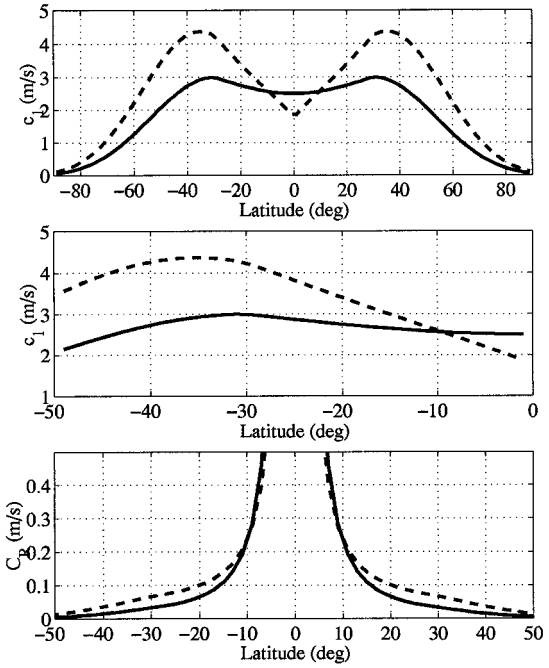

FIG. 9. Approximations to the first baroclinic mode gravity wave speeds, $c_1(\varphi)$, and the long Rossby wave speeds, $C_R(\varphi)$. The upper panel shows both the polynomial representation of the theoretical gravity wave speeds (Chelton et al. 1998) as a function of latitude (bold line), determined from the distribution of temperature and salinity, and the *effective* gravity wave speeds used in the model (dashed line), as determined from the observed long Rossby wave speeds from the TOPEX/Poseidon satellite altimeter (Chelton and Schlax 1996). The middle panel is an enlargement of the upper panel, for the latitudes of interest to this study. The lower panel shows the theoretical long Rossby wave speeds (bold line) as determined from the theoretical gravity wave speeds above, and the observed long Rossby wave speeds (dashed line) found by multiplying the ratio of the effective and theoretical gravity wave speeds by the theoretical long Rossby wave speed (cf. Fig. 5b of Chelton and Schlax 1996).

wave speed. There are good reasons for increasing the Rossby wave speed. The altimeter-based observations, filtered on different time and space scales to our results, show that the observed Rossby waves are approximately twice the speed of the expected long-wave speeds from conventional linear theory south of 20°S (Fig. 9). In addition, annually forced baroclinic long waves, driven by spatially uniform wind stresses, are expected to propagate westward at twice the phase speed of free nondispersive Rossby waves with the same period (White 1977). More recently, theoretical work on long Rossby waves also shows that the second and third baroclinic modes have a very important effect on the structure of the vertical shear that results in an increase by up to a factor of 2 in the apparent Rossby wave speed in the subtropics (Killworth et al. 1997).

Here, we present results from the numerical model driven by the Hellerman and Rosenstein winds. Figure 10 shows the distribution of *depth* anomalies of the internal surface from the annual mean [defined here as the *negative* of Eq. (2)] for the months of April, June,

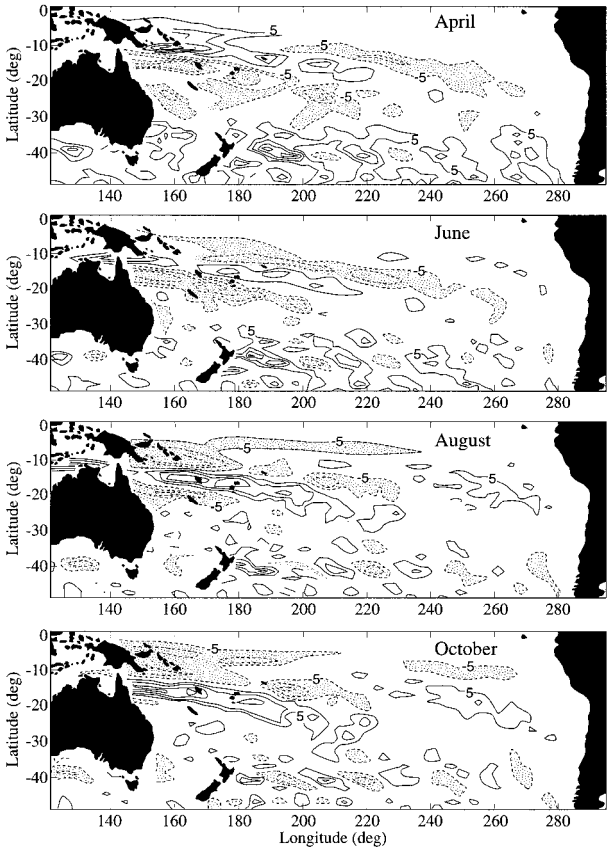

FIG. 10. Monthly internal surface depth (m) anomalies (from the annual mean) across the South Pacific Ocean for the months of April, June, August, and October. These results were simulated using the vorticity model forced with monthly mean wind stress curl anomalies across the width of the Pacific Ocean. The Rossby wave speeds at each latitude were scaled by a factor of 2.

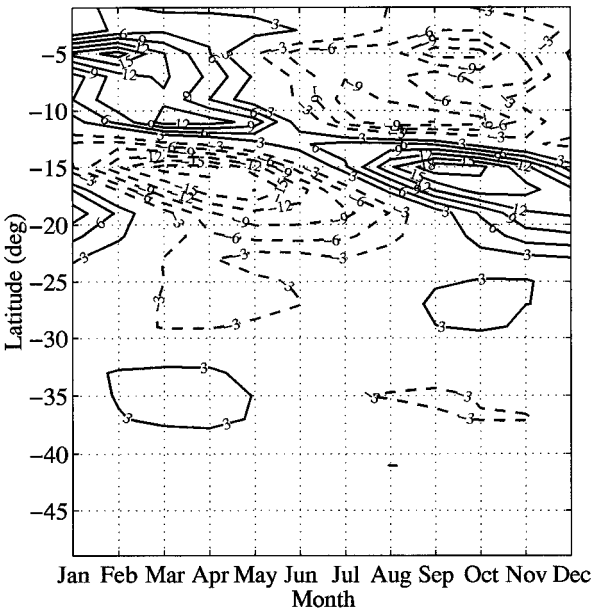

FIG. 11. Hovmöller plot of the zonally averaged internal surface depth anomalies (in meters) in the southwest Pacific Ocean calculated from the mass transport streamfunction as simulated by the numerical model and forced with monthly mean wind stress curl anomalies from the annual mean across the width of the Pacific Ocean. Here, a positive internal surface depth anomaly implies a depressed thermocline and corresponds to a raised sea surface height (positive anomaly of the free surface), i.e., greater heat content in the upper ocean and warmer temperature anomalies below the mixed layer. The Rossby wave speeds have been scaled by a factor of 2.

August, and October across the South Pacific Ocean. These results are from a simulation with the Rossby wave speeds scaled by a factor of 2 ($2 \times C_R$). With this scaling of the Rossby wave speeds in the simulation, the model gives a better representation of the spatial scales observed in the upper-ocean temperature data for the southwest Pacific region. From this figure, it is clear that there is westward propagation of an elongated (''sausage'' shaped) structure of wave anomalies, which extends in a west-northwest to east-southeast orientation between about 10° and 25°S across the South Pacific Ocean. The approximate wavelength (horizontal scale) of this feature is in excess of 6000 km. This horizontal scale is roughly twice the width of the southwest Pacific region.

Following this wave propagation westward in time from April to October, the internal surface depth anomalies between 10° and 20°S in the southwest Pacific region are shallowest in April, whereas in October they are deepest. On reaching the southwest Pacific region, the amplitude of the internal surface depth anomalies in the southwest Pacific, which have been propagated into the region from farther east, have combined with the local forcing to increase the local amplitude.

Examination of the zonally averaged $2 \times C_R$ model results (Fig. 11) and data (Fig. 7) as three separate latitude bands, 0°–10°S, 10°–30°S and >30°S, provides a qualitative understanding of the similarities between the model results and observations. From this comparison, the greatest similarity is across the latitude band 10°–30°S.

The phase of the internal surface depth variations is consistent with the phase of the variations in the depth of the 14°C isotherm at all latitudes between 10°S and 30°S. In this zonal band, which covers much of the subtropical gyre, the negative D14°C anomalies (subsurface cooling) in the early part of the year are qualitatively well represented by the negative internal surface depth anomaly pattern for the same latitudes and months in the model output. Similarly, the positive D14°C anomalies (subsurface warming) from July to November/December in the same region, are also well represented by the positive internal surface depth anomaly pattern given in the corresponding model results. Overall, the maximum amplitudes are such that the thermocline is shallowest (minimum depth) in March–April and deepest (maximum depth) in September–October. Thus, on these large spatial scales, the linear vorticity model predicts reasonably well the observed pattern of

climatological monthly thermocline variations for the subtropical gyre.

The amplitudes of both the zonally averaged internal surface depth variations and the surface height anomalies are also similar to the observations. Figures 11 and 7 both show that the maximum depth anomalies of the internal surface (thermocline) are about ± 15 m in the band 15°–20°S. Similarly, the amplitudes of the surface height anomalies (not shown) are consistent with the amplitudes of the zonally averaged dynamic height anomalies at 100-m depth relative to 450 m; that is, both have seasonal amplitudes of about ± 4 cm. Overall, it is clear that this simple vorticity model predicts quite well the observed ranges in both the internal surface depth anomalies and the dynamic height anomalies between 10° and 30°S for this enhanced Rossby wave speed.

In order to examine the dependence of the model results on the long Rossby wave speed (via the first baroclinic mode gravity wave speed, c_1) in the southwest Pacific arm of the subtropical gyre, 12 separate model simulations were performed by scaling the Rossby wave speed, C_R [through scaling β in Eq. (4)]. For experiments 1–12, C_R values were, respectively, scaled by factors of 0.01, 0.1, 0.5, 1, 1.5, 2, 2.5, 3, 3.5, 4, 5, and 10. Along 19°S, for example, the 12 scaled long Rossby wave speeds were, respectively, 0.001, 0.011, 0.053, 0.106, 0.158, 0.211, 0.264, 0.316, 0.369, 0.422, 0.527, and 1.055 m s^{-1}. In the case where scaled Rossby wave speeds approach 0 m s^{-1}, the linear vorticity model simulation becomes the familiar Ekman velocity.

Figure 12 shows the zonally averaged (a) internal surface depth and (b) surface height anomalies (meters) along 35°S, 29°S, 19°S, and 9°S in the southwest Pacific as a function of experiment number (Rossby wave speed) and month. For the gyre latitudes of 29° and 19°S the phase of the internal surface depth anomalies best represents the phase of the D14°C anomalies (Fig. 7) when the model is scaled by (2–2.5) $\times$ C_R (experiments 6–7). For 19°S, not only the phase but also the amplitude of the internal surface depth anomalies matches the D14°C anomalies at this latitude very well. Similarly at 29°S, also in the subtropical gyre, the phase agrees well for experiments 4–6 [i.e., (1–2) $\times$ C_R], but at this latitude, the amplitude is smaller than observed. Hence, for the higher latitudes within the subtropical gyre, the amplitude of the thermocline variations tends to be underestimated. South of the subtropical gyre, in the outflow of the East Australian Current (35°S), 4 $\times$ C_R (experiment 10) is the *only* scaling that results in internal surface depth variations that matches the D14°C phase variations seen in the observations.

Interestingly, for a number of latitudes, there appears to be resonance corresponding to a limited range of Rossby wave speeds. For example, at 19°S, as the Rossby wave speed increases from near zero (i.e., the Ekman solution), there is a slight increase in the magnitude of the internal surface depth anomalies at the satellite-observed Rossby wave speed [i.e., 1 $\times$ C_R (experiment 4), thus providing a slightly improved representation of the observed thermocline depth anomalies in the southwest Pacific region] followed by a sharp increase in magnitude to maximum values when the model is scaled by (2–2.5) $\times$ C_R (experiments 6–7). For higher Rossby wave speeds (experiments 8–12), the amplitude of the response decreases again. The peak in the response amplitude for 2.5 $\times$ C_R (experiment 7) at 19°S shows that the forced linear vorticity equation is close to resonance for this Rossby wave speed. Similar features are observed for (2.5 and 5) $\times$ C_R (experiments 7 and 11) at 35°S and for 1 $\times$ C_R (experiment 4) at 9°S.

The first experiment (0.01 $\times$ C_R) represents the case where the vorticity equation degenerates to the local Ekman velocity since Rossby wave propagation becomes negligible. At 19°S, the amplitude of the Ekman pumping on the internal and free surface is quite small, about 6 m and 0.02 m, respectively. Clearly, the inclusion of long Rossby waves (experiment 4 and particularly experiments 6–7) has amplified the internal surface depth and free surface height anomalies by a factor of 2 to 3 and consequently makes an important contribution to the amplitude of these anomalies. In addition, the *phase* of the internal surface depth response at 2.5 $\times$ C_R is effectively the same as that for $C_R \rightarrow 0$ at this latitude. This result holds true for the whole of the subtropical gyre where the observed amplitudes of the D14°C isotherm are larger than that expected from the pure Ekman solution, yet have the same phase as the Ekman solution. This gives rise to the important result that a purely local analysis is unable to distinguish the contribution of Ekman pumping and Rossby waves to the changes of the thermocline depth in the subtropical gyre, except through the amplitude of the response.

At 35°S, however, the observed D14°C anomalies are 180° out of phase with the local wind stress curl. Clearly, for this latitude, the phase of the anomalies is not consistent with local Ekman pumping. Furthermore, for the 2.5 $\times$ C_R case (experiment 7), the modeled variations of the depth of the internal surface at 35°S are also about 3 months out of phase with the D14°C anomalies; that is, the modeled anomalies lead the observations by about 3 months. In contrast, for 4 $\times$ C_R (experiment 10), the phase of the modeled anomalies better represents the observations. Hence, for this higher latitude, the much larger scaling of the Rossby wave speed performs much better.

b. Three-dimensional model simulations

Comparisons between the observations in the southwest Pacific and results from three-dimensional dynamical models further support the results in the simple vorticity model for the subtropical gyre. Results from model simulations discussed here are those generated using the Large Scale Geostrophic (LSG) model (Maier-Reimer et al. 1993) and the marginally eddy-resolving

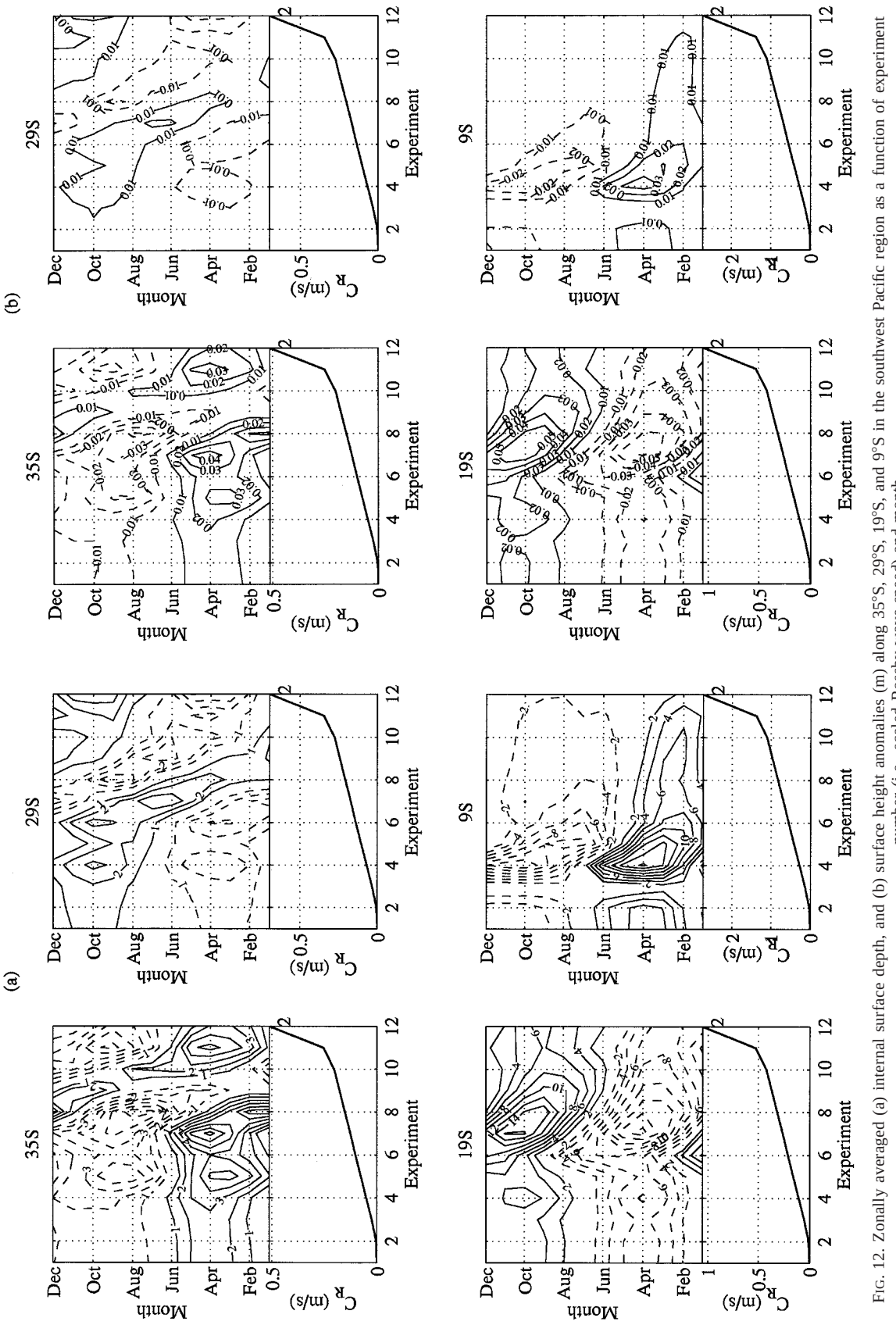

FIG. 12. Zonally averaged (a) internal surface depth, and (b) surface height anomalies (m) along 35°S, 29°S, 19°S, and 9°S in the southwest Pacific region as a function of experiment number (i.e., scaled Rossby wave speed) and month.

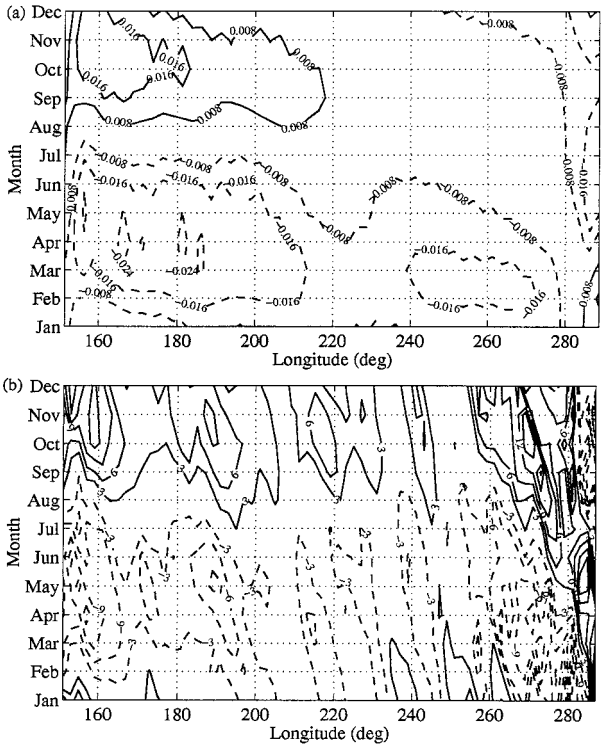

FIG. 13. Hovmöller plots, along 19°S, of (a) sea level anomalies (in meters) from the LSG model, and (b) D14°C anomalies determined from the POCM. Positive sea level anomalies indicate that sea level is higher, whereas positive D14°C anomalies contribute dynamically to a raised sea level.

Parallel Ocean Climate Model (POCM) of Semtner and Chervin (Semtner and Chervin 1988; Semtner and Chervin 1992).

In the LSG model simulation, the model was forced with climatological seasonal wind stresses, surface heat, and freshwater fluxes. The wind forcing is the same as that used to drive the linear vorticity model. The role of the heat and freshwater fluxes on the predicted sea level was diagnosed and removed, leaving the seasonal wind-driven component of the sea level variations (Bindoff et al. 1997). Figure 13a shows a Hovmöller plot of sea surface height anomalies along 19°S over the seasonal cycle. At this latitude, the zonal scale is large and coherent from the East Australian coast to 180°. The amplitude of the changes over this region are about half of that inferred from the dynamic height variations (i.e., at 100-m depth relative to 450-m depth), determined using a constant salinity. However, the phase is very consistent with the observations, with the maximum upwelling of the thermocline causing a sea level minimum to occur in March–May and the maximum depression of the thermocline causing a sea level maximum to occur in late October. This pattern of change over the subtropical gyre in the model is quite similar to that observed over the subtropical gyre in the observations.

Results from a separate analysis of monthly averaged D14°C anomalies from a simulation over the 1980–89 decade using the POCM forced with daily European Centre for Medium-Range Weather Forecasts wind stresses (Chervin et al. 1997) are also consistent with those seen in the simple linear vorticity model. In this analysis, a monthly climatology was generated from the POCM output between 1983 and 1989 by averaging all seven Januarys, seven Februarys, etc., in an analogous way to the observations, the first three years of the simulation being ignored due to anomalies associated with the model spinup (A. Craig 1996, personal communication). The model climatology is, therefore, less averaged than the observations, which have data for 34 yr. Figure 13b shows the seasonal cycle of D14°C anomalies along 19°S for this 3D model. These results, for the gyre, are again similar to those for both the LSG and vorticity models, with the maximum negative (positive) amplitudes in March–May (October–December). The main difference here between the POCM and LSG model results is that wave peaks and troughs can be clearly seen in the figure. The wavelength of these waves along 19°S (about 30° of long), is consistent with the observed first baroclinic mode Rossby wave (and speeds) for this latitude (0.106 m s^{-1}, see Fig. 9) derived from the TOPEX/Poseidon satellite altimeter observations (Chelton and Schlax 1996). Furthermore, despite the amplitude of these POCM thermocline depth variations being about a factor of 2 smaller than the observations, the longitudinal structure of the peak amplitudes in the model results for the southwest Pacific region, in particular the dominant wave peaks seen just to the west of 160°E (Fig. 13b), is remarkably similar to the structure of D14°C anomalies at these longitudes (and latitude) in the observations for March and October (cf. Fig. 6).

5. Discussion and conclusions

In this paper, thermocline depth (D14°C/D13°C) anomalies, derived from a new atlas of monthly mean upper-ocean temperatures for the southwest Pacific Ocean, were used to investigate the phase and amplitude of the seasonal changes in the depth of the thermocline for this region. In this study, it was found that vertical movements of the thermocline, and hence also seasonal temperature anomalies below the surface mixed layer in the subtropical southwest Pacific, were out of phase with the annual cycle of solar insolation.

Interestingly, these thermocline movements were not expressed in the surface dynamic height fields relative to 450-m depth. Similarly, monthly mean sea level data at various sites in this region describe sea level changes that are also typically *in phase* with seasonal variations in the insolation of the surface mixed layer, but again fail to represent the anticorrelation with observed subsurface temperature anomalies (due to movements of the thermocline) in the southwest Pacific as described

in this study. These thermocline variations are masked in both the 0–450 m dynamic height and sea level fields by the integrated effects of the vertical temperature changes in the upper ocean, which are dominated by seasonal solar heating of the surface mixed layer. Hence, upper-ocean circulation variability in the subtropics and midlatitudes of the southwest Pacific Ocean cannot be properly understood without in situ observations of temperature changes below the surface mixed layer.

To further examine the seasonal relationship between thermocline movements in the southwest Pacific region and the contribution from both the local and remote wind stress curl, a simple time-dependent numerical model was developed based on the linear vorticity equation and was forced with observed wind stresses across the entire South Pacific Ocean. Results from the vorticity model, with the inclusion of Rossby waves at the altimeter-observed phase speeds, C_R, showed a moderate improvement in the prediction skill of the vertical movements of the thermocline in the southwest Pacific region, as compared with the simple Ekman solution. Furthermore, it was found that the observed thermocline variability in the southwest Pacific was represented much better by the model using Rossby wave speeds of $(2–2.5) \times C_R$.

Overall, the results from these model simulations for the subtropical gyre latitudes between about 10° and 30°S, with the inclusion of Rossby waves, were both qualitatively and quantitatively consistent with seasonal changes in the depth of the 14°C isotherm. It should be stressed that the numerical results for the subtropics of the southwest Pacific Ocean, generated using this purely dynamical model, were more consistent with the inclusion of both the time-varying and β (Rossby) terms in the vorticity equation. The role of the modified β term implies that Rossby waves are an important part of the dynamics in the region between Australia and 180°.

These findings are supported by results from numerical simulations using two separate three-dimensional models. In particular, the results from the Parallel Ocean Climate Model of Semtner and Chervin suggest that Rossby waves, at the phase speeds observed with the TOPEX/Poseidon altimeter, are important to the overall structure of the thermocline depth anomalies in the subtropical gyre region of the southwest Pacific.

Acknowledgments. Helpful comments were provided by Dr. Charles Macaskill from the School of Mathematics and Statistics, University of Sydney, New South Wales, Australia; Dr. Richard Coleman from the School of Geography and Environmental Studies, University of Tasmania, Hobart, Tasmania, Australia; Dr. Joerg-Olaf Wolff from the Antarctic CRC, University of Tasmania, Hobart, Tasmania, Australia; and Dr. Susan Wijjfels from the CSIRO Division of Marine Research, Hobart, Tasmania, Australia. This paper also benefitted greatly from comments by Dr. Stuart Godfrey from the CSIRO Division of Marine Research and one anonymous reviewer. The POCM data were generously provided by Dr. Robert Chervin from the National Center for Atmospheric Research (NCAR), Boulder, Colorado, and Dr. Albert Semtner Jr. from the Naval Postgraduate School, Monterey, California. The authors are also grateful to Mr. Anthony Craig from NCAR, for his help with preparing the POCM data and Mrs. Judy Davis from the School of Earth Sciences, Macquarie University, North Ryde, New South Wales, Australia, for redrafting some of the computer-generated figures. This project was partly supported by a National Greenhouse Advisory Committee (NGAC) grant.

APPENDIX

Synthesis of Ocean Temperature Data

a. Singular value decomposition

Let $\mathbf{A}$ be an $M \times N$ matrix for the data such that M represents the number of standard depths and N is the number of stations. Vertical positions are allocated every five meters from the surface to 450-m depth, making a total of 91 standard depths. Following Fukumori and Wunsch (1991), the temperature data are normalized by subtracting an a priori (first guess) mean and dividing by an a priori error. Hence, each element of the $\mathbf{A}$ matrix is described by

$$a_{ij} = \frac{T_{ij} - \overline{T_{ij}}}{\sigma_i}, \tag{A1}$$

where T_{ij} is the temperature value at depth i and station j, $\overline{T_{ij}}$ is the a priori mean at depth i and station j, and the normalization factor σ_i is the a priori error (noise) estimate at depth i.

The southwest Pacific region was divided such that each subregion still contained more than 8000 individual casts. Consequently, the number of stations in any one subregion was always far greater than the number of standard depths. To minimize the size of the eigenvalue problem, the data matrix was constructed with depth in the row dimension. Hence, each column of the matrix contained a separate MBT/XBT cast corresponding to a geographic location and time. The singular value decomposition (SVD) was performed on the vertical covariance matrix $\mathbf{A}\mathbf{A}^{\mathrm{T}}$ for the data within each subregion. In mathematical terms,

$$\mathbf{A}\mathbf{A}^{\mathrm{T}} = \mathbf{U}\mathbf{\Lambda}^2\mathbf{U}^{\mathrm{T}}, \tag{A2}$$

where the columns, $\mathbf{u}_i$, of $\mathbf{U}$ are the vertical eigenvectors. Now, from the definition of the SVD of the data matrix, $\mathbf{A}$,

$$\mathbf{A} = \mathbf{U}\mathbf{\Lambda}\mathbf{V}^{\mathrm{T}}, \tag{A3}$$

a simple rearrangement, using the orthogonality property of $\mathbf{U}$ (i.e., $\mathbf{U}^{-1} = \mathbf{U}^{\mathrm{T}}$), yields

$$\mathbf{V} = (\mathbf{\Lambda}^{-1}\mathbf{U}^{\mathrm{T}}\mathbf{A})^{\mathrm{T}}, \tag{A4}$$

where the diagonal elements of the $M \times M$ matrix $\mathbf{\Lambda}$

are the set of singular values (effectively the eigenvalues) and $\mathbf{V}$ is an $N \times M$ matrix with each column vector $\mathbf{v}_i$, representing the amplitudes of the associated vertical eigenvector $\mathbf{u}_i$. Since each column of the data matrix $\mathbf{A}$ represents a single cast corresponding to a geographic location and time, each column vector $\mathbf{v}_i$ represents the time and space variation of the associated vertical eigenvector $\mathbf{u}_i$.

The rank, p, of the matrix $\mathbf{A}$, is the minimum dimension of $M \times N$ and represents the total number of modes, that is, equal to the total number of eigenvectors or eigenvalues arising from the SVD. Here, we are primarily interested in the number of significant modes, $k \leq p$, which are above the noise level in the data. Hence, these k modes are retained and only the elements in the first k vectors, $\mathbf{v}_i$, are objectively mapped in space and time onto a regular grid (discussed in the appendix part *d*).

b. A priori mean field

The a priori mean field was calculated as a polynomial fit to the entire temperature dataset for the southwest Pacific. This mean field is modeled as a second-order polynomial in latitude and depth and with an annual and semiannual harmonic in time yielding a total of 45 regression coefficients including cross-correlation terms. The resulting a priori mean field was used as the first-guess mean field estimate in the EOF analysis.

c. A priori noise

On these relatively large spatial scales, noise is defined as the small-scale variability associated with mesoscale eddies, internal waves, and other unresolved ocean processes. The variance of the data about its mean vertical structure contains both the signal variance and the noise variance, and is not necessarily an appropriate measure for σ_i. A better estimate of the noise variance at each depth is found from the difference between each temperature value and those for neighboring casts. ''Neighboring'' is referred to here as the shorter scales that tend to separate individual casts along a cruise track spatially by less than 100 km and temporally by less than 1 day, and may comprise repeated sampling of individual eddies.

Let T_r be the observed temperature for cast r at a selected depth and T_s be the temperature value of a neighboring cast at the same depth. The noise variance is defined as

$$\sigma_i^2 = \frac{1}{2N} \sum_{k=1}^{N} (T_r - T_s)_k^2, \tag{A5}$$

where $(T_r - T_s)_k$ is the kth difference between pairs of distinct casts separated spatially by less than 100 km and temporally by less than 1 day [see Fukumori and Wunsch (1991)]. The a priori noise estimates calculated at each depth with this equation were used to normalize the temperature differences in the EOF analysis and to scale the error fields associated with the gridded temperature maps arising from the objective mapping.

d. Objective mapping

Objective mapping is used to map each of the retained $\mathbf{v}_i$ onto the chosen regular horizontal grid. The vertical structure at each grid point for each mapped mode is defined by $\mathbf{u}_i$. The objectively mapped $\mathbf{v}_i$ values are given by Bretherton et al. (1976) as

$$\mathbf{v}_{i_{\text{grid}}} = \mathbf{C}_{i_{md}} \mathbf{C}_{i_{dd}}^{-1} (\mathbf{v}_i - \overline{\mathbf{v}_i}) + \overline{\mathbf{v}_i}, \tag{A6}$$

where $\mathbf{v}_i$ is the ith eigenvector of the horizontal coefficient matrix, $\overline{\mathbf{v}_i}$ is the mean of the coefficients for the ith mode, and $\mathbf{C}_{md}$ and $\mathbf{C}_{dd}$ are, respectively, the model–data and data–data covariance matrices.

An anisotropic Gaussian covariance function (including time) was chosen for the analysis. Each element of the data–data covariance matrix $\mathbf{C}_{i_{dd}}$ is given by

$$C_{i_{dd}} = s_i \exp\left\{ -\left(\frac{\Delta r_{x_{jk}}}{l_x}\right)^2 - \left(\frac{\Delta r_{y_{jk}}}{l_y}\right)^2 - \left(\frac{\Delta r_{t_{jk}}}{l_t}\right)^2 \right\} + e_i \delta_{jk}, \tag{A7}$$

where $\Delta r_{x_{jk}}$, $\Delta r_{y_{jk}}$, $\Delta r_{t_{jk}}$ are the distances (degrees) in longitude, latitude, and time (days), respectively, between data points j and k; l_x, l_y, l_t are the corresponding covariance scales; and s_i and e_i are estimates of the signal and noise variances for the ith mode, respectively. The noise variance (e_i) of $\mathbf{v}_i$ is obtained using the same procedure as for the a priori noise. The model–data covariance matrix $\mathbf{C}_{i_{md}}$ is described by an equation almost identical to Eq. (A7), the only difference being that the Kronecker delta term is not included. Here, the identities $\Delta r_{x_{jk}}$, $\Delta r_{y_{jk}}$, $\Delta r_{t_{jk}}$ are the distances (degrees) in longitude, latitude and time (days), respectively, between a data and model grid point.

The nondimensional error, $\sigma_{ij_{\text{norm}}}$, is reconstructed using the relation

$$\sigma_{ij_{\text{norm}}}^2 = \sum_{m=1}^{k} (u_{im} \lambda_m e_{jm})^2, \tag{A8}$$

where k is the number of modes for the reconstruction and u_{im} and e_{jm} are, respectively, the mth mode eigenvector and estimated error of the mapped coefficients at the jth grid point and at the ith depth (cf. Bretherton et al. 1976). Consequently, the dimensional error is represented by

$$\hat{\sigma} = \sigma_{\text{norm}} \sigma_{\text{apriori}}. \tag{A9}$$

This estimate of the error is incomplete since it does not account for the error associated with the neglected modes.

Computationally, the objective mapping procedure is costly. The procedure involves an inversion of the data–data covariance matrix. This is an N^3 operation in time and becomes almost unmanageable for $N > 1500$ points,

or so, on most good workstations. A major advantage of the EOF analysis procedure combined with objective mapping is that it reduces the number of times that mapping is required while still retaining the three-dimensional correlations present in the data.

In this analysis, monthly mean temperature fields on a $2° \times 2°$ grid were generated in order to describe the seasonal variability in the temperature data collected between 1955 and 1988. To generate these gridded monthly means, the data were organized into 12 months of length ''365.25/12 days.'' To a close approximation, all January data were organized into one group, all February data into another group, and so on.

The objective mapping procedure relies on a reasonable choice of scales based on both the underlying physics and the data distribution. Here, horizontal length scales of $2°$ lat $\times$ $4°$ long and a timescale of 90 days were chosen. The larger scales in longitude were chosen due to the zonality of ocean temperatures and the choice of grid was selected to be consistent with the wind stresses.

REFERENCES

Andrews, J. C., M. W. Lawrence, and C. S. Nilsson, 1980: Observations of the Tasman Front. *J. Phys. Oceanogr.,* **10,** 1854–1869.

Bindoff, N. L., and C. Wunsch, 1992: Comparison of synoptic and climatologically mapped sections in the South Pacific Ocean. *J. Climate,* **5,** 631–645.

——, R. Coleman, H. van Gysen, and J. O. Wolff, 1997: The role of heat fluxes and winds on seasonal sea-level signals. *Global Geodynamics Coupled with Variations of Atmosphere and Ocean,* M. Ooe, Ed., Division of Earth Rotation, National Astronomical Observatory, Japan, 45–57.

Boland, F. M., 1971: Temperature–salinity anomalies at depths between 200 m and 800 m in the Tasman Sea. *Aust. J. Mar. Freshwater. Res.,* **22,** 55–62.

——, and J. A. Church, 1981: The East Australian Current 1978. *Deep-Sea Res.,* **28A,** 937–957.

Bretherton, F. P., R. E. Davis, and C. B. Fandry, 1976: A technique for objective analysis and design of oceanographic experiments applied to MODE-73. *Deep-Sea Res.,* **23,** 559–582.

Chelton, D. B., and M. G. Schlax, 1996: Global observations of oceanic Rossby waves. *Science,* **272,** 234–238.

——, R. A. deSzoeke, M. G. Schlax, K. El Naggar, and N. Siwertz, 1998: Geographical variability of the first baroclinic Rossby radius of deformation. *J. Phys. Oceanogr.,* **28,** 433–460.

Chervin, R. M., A. P. Craig, and A. J. Semtner, 1997: Meridional heat transport variability from a global eddy-resolving ocean model. *Assessing Climate Change: Results from the Model Evaluation Consortium for Climate Assessment.* Gordon and Breach Science Publishers, 143–168.

Church, J. A., 1987: East Australian Current adjacent to the Great Barrier Reef. *Aust. J. Mar. Freshwater Res.,* **38,** 671–683.

——, and F. M. Boland, 1983: A permanent undercurrent adjacent to the Great Barrier Reef. *J. Phys. Oceanogr.,* **13,** 1747–1749.

De Mey, P., and A. R. Robinson, 1987: Assimilation of altimeter eddy fields in a limited area quasi-geostrophic model. *J. Phys. Oceanogr.,* **17,** 2280–2293.

Fukumori, I., and C. Wunsch, 1991: Efficient representation of the North Atlantic hydrographic and chemical distributions. *Progress in Oceanography,* Vol. 27, Pergamon Press, 111–195.

Godfrey, J. S., 1989: A Sverdrup model of the depth-integrated flow for the World Ocean allowing for island circulations. *Geophys. Astrophys. Fluid Dyn.,* **45,** 89–112.

——, G. R. Cresswell, T. J. Golding, and A. F. Pearce, 1980: The separation of the East Australian Current. *J. Phys. Oceanogr.,* **10,** 430–440.

Haines, K., 1991: A direct method for assimilating sea surface height data into ocean models with adjustments to deep circulation. *J. Phys. Oceanogr.,* **21,** 843–868.

Hamon, B. V., 1965: The East Australian Current. 1960–1964. *Deep-Sea Res.,* **12,** 899–921.

Hellerman, S., and M. Rosenstein, 1983: Normal monthly wind stress over the World Ocean with error estimates. *J. Phys. Oceanogr.,* **13,** 1093–1104.

Holbrook, N. J., 1994: Temperature variability in the Southwest Pacific Ocean between 1955 and 1988. Ph.D. thesis, University of Sydney, 229 pp.

——, and N. L. Bindoff, 1997: Interannual and decadal temperature variability in the southwest Pacific Ocean between 1955 and 1988. *J. Climate,* **10,** 1035–1049.

Kessler, W. S., 1990: Observations of long Rossby waves in the northern tropical Pacific. *J. Geophys. Res.,* **95,** 5183–5217.

Killworth, P. D., D. B. Chelton, and R. A. de Szoeke, 1997: The speed of observed and theoretical long extratropical planetary waves. *J. Phys. Oceanogr.,* **27,** 1946–1966.

Lilley, F. E. M., J. H. Filloux, N. L. Bindoff, I. J. Ferguson, and P. J. Mulhearn, 1986: Barotropic flow of a warm-core ring from seafloor electric measurements. *J. Geophys. Res.,* **91,** 12 979–13 109.

Maier-Reimer, E., U. Mikolajewicz, and K. Hasselmann, 1993: Mean circulation of the Hamburg LSG OGCM and its sensitivity to the thermohaline surface forcing. *J. Phys. Oceanogr.,* **23,** 731–757.

Meyers, G., 1979: On the annual Rossby wave in the tropical North Pacific Ocean. *J. Phys. Oceanogr.,* **9,** 663–674.

Minster, J. F., C. Brossier, and P. Rogel, 1995: Variation of the mean sea level from TOPEX/Poseidon data. *J. Geophys. Res.,* **100,** 25 153–25 161.

Mulhearn, P. J., 1987: The Tasman Front: A study using satellite infrared imagery. *J. Phys. Oceanogr.,* **17,** 1148–1155.

——, J. H. Filloux, F. E. M. Lilley, N. L. Bindoff, and I. J. Ferguson, 1986: Abyssal currents during the formation and passage of a warm-core ring in the East Australian Current. *Deep-Sea Res.,* **33,** 1563–1576.

——, ——, ——, ——, and ——, 1988: Comparison between surface, barotropic and abyssal flows during the passage of a warm core ring. *Aust. J. Mar. Freshwater Res.,* **39,** 697–707.

National Oceanographic Data Center, 1991: CD-ROMs NODC-02 and NODC-03: Global ocean temperature and salinity profiles. Informal Report No. 11, National Oceanographic Data Center, Washington, DC, 14 pp. [Available from National Oceanographic Data Center, User Services Branch, NOAA/NESDIS E/OC21, 1825 Connecticut Ave., NW, Washington, DC 20235.]

Pearce, A., 1981: Temperature–salinity relationships in the Tasman Sea. Report 135, CSIRO Marine Laboratories, Cronulla, Australia, 41 pp. [Available from CSIRO Division of Marine Research Library, GPO Box 1538, Hobart TAS 7001, Australia.]

Philander, S. G. H., 1979: Variability of the tropical oceans. *Dyn. Atmos. Oceans,* **3,** 191–208.

Rebert, J. P., J. R. Donguy, G. Eldin, and K. Wyrtki, 1985: Relations between sea level, thermocline depth, heat content, and dynamic height in the tropical Pacific Ocean. *J. Geophys. Res.,* **90,** 11 719–11 725.

Reid, J. L., 1986: On the total geostrophic circulation of the South Pacific Ocean: Flow patterns, tracers and transports. *Progress in Oceanography,* Vol. 16, Pergamon Press, 1–61.

Ridgway, K. R., and J. S. Godfrey, 1994: Mass and heat budgets in the East Australian current: A direct approach. *J. Geophys. Res.,* **99,** 3231–3248.

Semtner, A. J., and R. M. Chervin, 1988: A simulation of the global ocean circulation with resolved eddies. *J. Geophys. Res.,* **93,** 15 502–15 522.

——, and ——, 1992: Ocean general circulation from a global eddy-resolving model. *J. Geophys. Res.*, **97,** 5493–5550.

Stammer, D., and C. Wunsch, 1994: Preliminary assessment of the accuracy and precision of TOPEX/Poseidon altimeter data with respect to the large scale ocean. *J. Geophys. Res.,* **99,** 24 584–24 604.

Tomczak, M., and J. S. Godfrey, 1994: *Regional Oceanography: An Introduction*. Pergamon Press, 422 pp.

White, W. B., 1977: Annual forcing of baroclinic long waves in the tropical North Pacific Ocean. *J. Phys. Oceanogr.,* **7,** 50–61.

Woodruff, S. D., R. J. Slutz, R. L. Jenne, and P. M. Steurer, 1987: A Comprehensive Ocean–Atmosphere Data Set. *Bull. Amer. Meteor. Soc.*, **68,** 1239–1250.

Woodworth, P. L., 1991: The permanent service for mean sea level and the global sea level observing system. *J. Coastal Res.*, **7,** 699–710.

Wyrtki, K., 1962: Geopotential topographies and associated circulation in the western South Pacific Ocean. *Aust. J. Mar. Freshwater Res.,* **13,** 89–105.